

See discussions, stats, and author profiles for this publication at: <https://www.researchgate.net/publication/278669799>

Density Functional Theory-Assisted Microkinetic Analysis of Methane Dry Reforming on Ni Catalyst

ARTICLE *in* INDUSTRIAL & ENGINEERING CHEMISTRY RESEARCH · JUNE 2015

Impact Factor: 2.59 · DOI: 10.1021/acs.iecr.5b00563

CITATION

1

READS

60

6 AUTHORS, INCLUDING:



Chen Fan

Queensland University of Technology

57 PUBLICATIONS 296 CITATIONS

[SEE PROFILE](#)



Yi-An Zhu

East China University of Science and Technology

32 PUBLICATIONS 342 CITATIONS

[SEE PROFILE](#)



De Chen

Norwegian University of Science and Technol...

237 PUBLICATIONS 4,798 CITATIONS

[SEE PROFILE](#)

Density Functional Theory-Assisted Microkinetic Analysis of Methane Dry Reforming on Ni Catalyst

Chen Fan,[†] Yi-An Zhu,^{*,†,‡} Ming-Lei Yang,[†] Zhi-Jun Sui,[†] Xing-Gui Zhou,[†] and De Chen^{*,§}

[†]UNILAB, State Key Laboratory of Chemical Engineering, and [‡]Shanghai Key Laboratory of Multiphase Materials Chemical Engineering, East China University of Science and Technology, Shanghai 200237, China

[§]Department of Chemical Engineering, Norwegian University of Science and Technology (NTNU), N-7491 Trondheim, Norway

Supporting Information

ABSTRACT: A comprehensive microkinetic model based on density functional theory (DFT) calculations is constructed to explore the reaction mechanism for dry methane reforming on Ni catalyst. Three low-index facets, namely, Ni(111), Ni(100), and Ni(211), are utilized to represent the contributions from the flat, open, and stepped surfaces. Adsorption energies of all the possible reaction intermediates as well as activation energies for the elementary reactions involved in dry reforming of methane on the three Ni surfaces are calculated through DFT. These results are further employed to estimate the rate constants for the elementary reactions under realistic temperatures and pressures within the framework of transition state theory and statistical mechanics treatments. The dominant reaction pathway is identified as CH₄ successive dissociation followed by carbon oxidation by atomic oxygen. The dependence of the rate-determining step on operating conditions is examined. At low CH₄ and CO₂ partial pressures, both CH₄ dissociative adsorption and carbon oxidation would jointly dominate the overall reaction rate, while at high pressures carbon oxidation is suggested as the rate-determining step for the DRM reaction. Our findings provide a rational interpretation of contradictory experimental observations.

1. INTRODUCTION

Dry reforming of methane (DRM) has attracted increasing attention in the past two decades.^{1–10} On one hand, this process converts two greenhouse gases, namely CH₄ and CO₂, to syngas. On the other hand, the produced syngas from dry reforming of methane has a lower H₂/CO ratio than that from steam reforming of methane, which can be preferentially used in the production of long-chain alkanes by Fischer–Tropsch synthesis.¹¹ The most attractive catalyst for DRM might be the supported Ni catalyst because of its relatively high activity and low cost. However, carbon deposition is a severe problem under the reforming conditions, which would lead to rapid deactivation of the catalyst. To improve the stability of the Ni catalyst and thus the economic efficiency of the DRM process, it is of vital importance to explore the reaction mechanism under realistic conditions by using detailed kinetic analysis. Without a clear understanding of the reaction mechanism, strategies to overcome the problem remain trial-and-error approaches.

Since there are a large number of elementary reactions involved in the DRM process, the overall reaction network of DRM is rather complicated, which makes it difficult to investigate the reaction mechanism. Although great efforts have been devoted to exploring the reforming mechanism for the DRM reaction over Ni-based catalyst, the detailed kinetics, including the dominant reaction pathway and rate-determining step (RDS) is still controversial and often contradictory.^{12–19} Bradford and Vannice¹⁹ proposed that CO₂ participates in the reaction mechanism through the reverse water–gas shift (RWGS) reaction to produce surface OH groups, and the OH groups react with the adsorbed CH_x ($x = 0–3$) species to yield a formate-type intermediate (CH_xOH), which further

decomposes to yield H₂ and CO. In their kinetic model, both CH₄ dissociation and CH_xOH decomposition were suggested to be the RDSs over supported Ni catalysts. The proposed reaction mechanism was confirmed by the later research work by Nandini et al. over a Ni–K/CeO₂–Al₂O₃ catalyst.¹⁶ On the other hand, using isotopic studies and forward rate measurements, Wei and Iglesia¹⁰ suggested that the adsorbed CH_x species are oxidized by atomic O to form the intermediates CH_xO, and the CH₄ dissociation was considered as the RDS. Luo et al.¹⁵ claimed that although the cleavage of C–H bonds is a slow step, the decomposition of CH_xO ($x = 1–2$) into CO and adsorbed H species is the RDS for the reforming reaction. The work by Osaki and Mori supported their conclusion, and the same RDS was identified over the K-promoted Ni catalysts.^{17,18} Chang et al. proposed that the oxidization of atomic C by surface O species is the RDS in the reforming reaction over a K–Ni–Ca catalyst.¹² Using steady-state and transient kinetic methods, Cui et al. investigated the mechanism for the DRM reaction over Ni/α-Al₂O₃ catalyst over a wide range of temperatures. They suggested that CH₄ dissociation was the RDS at low temperatures, while the reaction between CH_x and CO₂ became the RDS at high temperatures.¹³

It is well-known that microkinetic modeling at an atomic or molecular level is a powerful method for a detailed understanding of the reaction mechanism for the systems with a complicated reaction network.^{20–22} In particular, the dominant reaction pathway and RDS can be convincingly identified based

Received: February 8, 2015

Revised: May 8, 2015

Accepted: May 14, 2015

Published: May 14, 2015



on the reaction rates of elementary reactions which can be obtained directly from the simulated results. Because no RDS is assumed and the kinetic parameters are determined on a physical basis, microkinetic modeling proves to be more reliable than the conventional kinetic modeling where the RDS has to be assumed. Nevertheless, gathering the kinetic parameters for microkinetic modeling is still a great challenge because the activation energies and entropy changes for elementary reactions are difficult to be measured from conventional experimental techniques. Fortunately, this problem can be overcome by first-principles calculations based on density functional theory (DFT), which have been frequently used to calculate adsorption heats and activation energies in heterogeneous catalysis.^{23,24} The calculated results are often in reasonable agreement with available experimental data. With the combination of the DFT results and the statistical thermodynamic treatments, the rate constants for the elementary reactions can be obtained and the microkinetic model can be constructed accordingly. Such an approach has already been applied to various catalytic reaction systems, such as steam methane reforming,^{20,21} crotonaldehyde hydrogenation,^{25,26} and NO oxidation.²⁷ These kinetic studies indicated that the DFT-assisted microkinetic modeling can provide semiquantitative or quantitative kinetic understanding of reaction mechanisms with great clarity and simplicity.

In our previous work, the adsorption energies of the reactants, intermediates, and products, and the activation energies for the elementary reactions involved in the DRM process were calculated over the close-packed Ni(111) surface.²⁸ A multifaceted microkinetic model has also been developed for steam methane reforming.²¹ In the present work, we set up a multifaceted microkinetic model for dry methane reforming, for which kinetic parameters on Ni(111), Ni(100), and Ni(211) are estimated by DFT. This contribution is structured as follows. The surface models and computational details are first introduced. The DFT-calculated adsorption energies of the possible reaction intermediates and activation energies for the elementary reactions involved in the DRM reaction are then presented. After that, the rate constants for the elementary reactions are obtained within the framework of statistical mechanics treatment and transition state theory, on the basis of which a full microkinetic model is constructed to identify the dominant reaction pathways leading to the formation of synthesis gas, the contribution of each reaction pathway to the overall reaction kinetics, and the RDS for each reaction pathway. Finally, the dependence of the DRM reaction mechanism, especially the RDS, on operating conditions is discussed, which provides a rational interpretation of the contradictory experimental findings.

2. COMPUTATIONAL DETAILS

In this work, all the DFT calculations were performed with the VASP code in which the wave functions at each k-point are expanded with a plane wave basis set with a kinetic cutoff energy up to 400 eV.^{29–32} The interactions between valence electrons and ion cores were treated by Blöchl's all-electron-like projector augmented wave method (PAW).^{33,34} The exchange-correlation functional utilized was the generalized gradient approximation functional proposed by Perdew, Burke, and Ernzerhof, known as GGA-PBE.³⁵ Brillouin zone sampling was performed using a Monkhorst-Pack³⁶ grid, and electronic occupancies were determined according to a Methfessel–Paxton scheme with an energy smearing of 0.2 eV.³⁷ Because

there is a magnetic elements (Ni) involved in the system, spin polarized effects were considered. Our previous calculations showed that surface magnetism is essential for an accurate quantitative description of the total energies.³⁸

Three low-index facets including Ni(111), Ni(100), and Ni(211) were utilized to model the surface of face-centered cubic (FCC) Ni nanoparticles. The model for Ni(111) was the same as that in our previous work.²⁸ The Ni(100) surface was modeled by a four-layer slab with a $p(3 \times 3)$ supercell. A vacuum layer as large as 12 Å was used along the direction of the surface normal to avoid periodic interactions. The first Brillouin zone of the $p(3 \times 3)$ supercell was sampled with a Γ -centered $3 \times 3 \times 1$ k-grid, which proved to be sufficient for this cell. The bottom two layers in the slab were fixed and the top two layers as well as the adsorbates were allowed to relax during geometry optimization and transition state search. To simulate the stepped Ni(211) surface, a $p(1 \times 3)$ supercell with 13 layers of Ni atoms was used. The bottom six layers were fixed, and the first Brillouin zones of the $p(1 \times 3)$ supercell was sampled with a Γ -centered $4 \times 3 \times 1$ k-grid.

The dimer method was used to locate the TSs for all the surface reactions.³⁹ In all the calculations, a force-based conjugate gradient method was used to optimize geometries.⁴⁰ Saddle points and minima were considered to be converged when the maximum force in every degree of freedom was less than 0.03 eV/Å. To verify the configurations of adsorption and TSs, vibrational frequency calculations were carried out by the numerical finite difference method. To obtain accurate forces, the total energy and band structure energy were converged to within 1×10^{-7} eV/atom during electronic optimization.

The adsorption energies of the adsorbates were calculated by

$$E_{\text{ads}} = E_{\text{adsorbate/surface}} - E_{\text{surface}} - E_{\text{adsorbate}} \quad (1)$$

where the first term on the right-hand was the total energy of the surface with the adsorbate adsorbed, the second term the total energy of the bare surface, and the last term the total energy of an isolated adsorbate. The first two terms were calculated with the same parameters (k-point sampling, energy cutoff, etc.). The third term was calculated by putting the isolated adsorbate in a box with dimensions of 15 Å × 15.5 Å × 16 Å and carrying out a spin-polarized Γ -point calculation. Under this definition, a more negative value of adsorption energy denotes stronger binding between adsorbate and surface.

3. RESULTS AND DISCUSSION

3.1. DFT Study of DRM. **3.1.1. Adsorption of Reactants, Intermediates, and Products.** As proposed in our previous work and illustrated in Figure 1,²⁸ the DRM process has a large reaction network. In this network, the following steps are included: (i) CH₄ molecules adsorb and dissociate to CH_x ($x = 0–3$) species and atomic H on the catalyst surface; (ii) Chemisorbed CO₂ dissociates to CO and O, or reacts with adsorbed H to form COOH or HCOO, which can be further decomposed into CO and OH (or CHO and atomic O). (iii) CH_x ($x = 0–3$) species react with surface OH or O to form CH_xOH or CH_xO intermediates, and CH_xOH or CH_xO decomposes into CO and H. (iv) CO and H₂ desorb to the gas phase as products. Within the whole reaction network, there are also some side reactions, that is, OH groups may further react with H to form H₂O, and the latter could desorb to the gas phase as a side product.

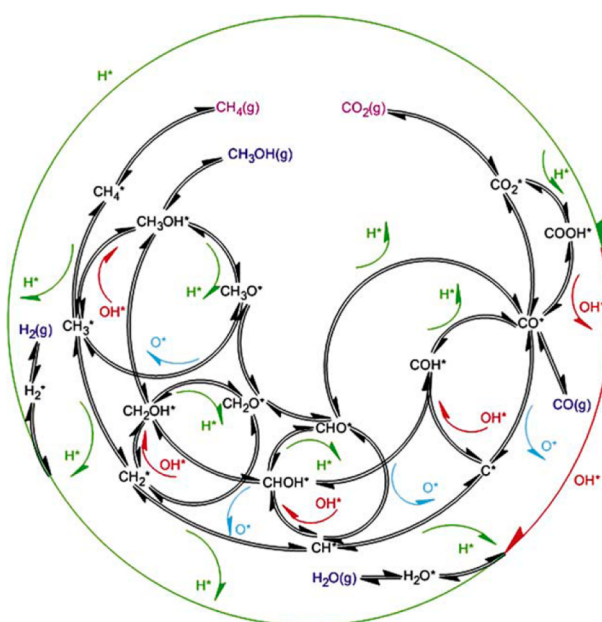


Figure 1. Reaction network for DRM over Ni catalyst. Reproduced with permission from ref 28. Copyright 2009 Elsevier.

The calculated adsorption energies of all the reactants, intermediates, and products in the DRM process on Ni(100) and Ni(211) are summarized in Table 1. The adsorption

Table 1. Adsorption Energies of Reactants, Intermediates, and Products in DRM on Ni(111),²⁸ Ni(100), and Ni(211)

no.	species	E_{ads} (eV)		
		Ni(111) ²⁸	Ni(100)	Ni(211)
1	CH ₄	-0.02	-0.02	-0.03
2	CH ₃	-1.91	-1.87	-2.20
3	CH ₂	-4.01	-4.32	-4.12
4	CH	-6.43	-7.06	-6.74
5	C	-6.78	-8.22	-7.83
6	H	-2.81	-2.75	-2.82
7	O	-5.67	-5.98	-5.81
8	OH	-3.42	-3.62	-3.88
9	H ₂ O	-0.29	-0.38	-0.54
10	H ₂	-0.22	-0.35	-0.37
11	CH ₃ OH	-0.30	-0.41	-0.48
12	CH ₂ OH	-1.54	-1.75	-2.06
13	CHOH	-3.88	-3.12	-4.11
14	COH	-4.39	-4.72	-4.43
15	CH ₃ O	-2.63	-2.84	-2.75
16	CH ₂ O	-0.75	-1.34	-1.17
17	CHO	-2.26	-2.85	-2.55
18	CO	-1.92	-1.95	-1.97
19	CO ₂	-0.02	-0.31	-0.28
20	COOH	-2.26	-2.73	-2.32
21	HCOO	-2.86	-3.16	-3.48

energies on Ni(111) taken from our previous work are also listed in Table 1 for comparison.²⁸ The corresponding adsorption configurations are shown in Figure 2 and Figure 3. From Table 1, one can see that the adsorption energies of the reaction intermediates on Ni(100) and Ni(211) are more negative than those on Ni(111). This is consistent with the universal agreement that under-coordinated sites are more

reactive than the high-coordinated sites and thus bind the adsorbates more strongly. When the adsorption energies on Ni(100) are compared to those on Ni(211), however, no simple trend can be found, that is, some species prefer to adsorb on Ni(100), while the others prefer Ni(211). This can be related to the geometries of the adsorption configurations. From Figures 2 and 3, one can see that for the species that favor the 4-fold hollow sites on Ni(100), such as, CH₂, CH, C, O, COH, and CH₃O, the adsorption on Ni(100) is stronger than that on Ni(211), while for those which favor the atop or bridge site, such as CH₃, H₂O, CH₃OH, CH₂OH, and CHOH, the adsorption on Ni(211) is stronger.

3.1.2. Activation Energies for Elementary Steps. After calculating the adsorption energies, we move on to compute the activation energies for the elementary reactions involved in the DRM process on Ni(211) and Ni(100), as summarized in Table S1 in the Supporting Information. The activation energies on Ni(111) taken from our previous work are also listed in Table S1 for comparison.²⁸ The corresponding TS structures can be found in the Supporting Information (Table S2). From Table S1, one can see that the activation energies for the elementary reactions vary substantially from surface to surface. These reactions can be classified into two categories: one is the bond-breaking reactions, for example, the dehydrogenation reactions, and the other is the bond-formation reactions, such as the oxidation reactions. For the bond-breaking reactions, the stronger is the adsorption of the reactants on the surface, the lower are the activation energies, and for the bond-formation reactions the activation energies are higher if the reactants are bound more strongly to the catalyst surface. These results are in reasonable agreement with the so-called Brønsted–Evans–Polanyi (BEP) relationship,^{41,42} which claims that the activation energy for an elementary reaction scales linearly with the reaction heat. That is, the kinetics of any catalytic reaction is to some extent controlled by the thermodynamics of the reaction. In other words, one would expect that the thermodynamically favored elementary reaction is faster. To examine the effect of thermodynamics on the kinetics for DRM, the activation energies for the elementary reactions on the three surfaces are plotted against the reaction heats, as shown in Figure 4.

It is apparent from the figure that no single BEP relation can be established for all the surface reactions. The upper-left region is dominated by the C–O bond-formation reactions, which are mainly the oxidation reactions of CH_x by O(H) to form CH_xO(H). The bottom-right region is mainly about the C–H bond-breaking reactions, which are the dehydrogenation reactions of CH_x or CH_xO(H). The area in-between is for the O–H bond-formation (or bond-breaking) reactions, which are related to the dehydrogenation of the CH_xOH species at the hydroxyl group or the formation of the OH and H₂O. In each region, however, the BEP relation holds roughly true. As the C–O, O–H, and C–H bonds are known to have different polarities, the plots show that the kinetics not only depends on the thermodynamics, but also is controlled by the intrinsic bond polarity. Similar trends have been reported in the previous publications on ethanol oxidation²³ and propane dehydrogenation⁴³ over Pt catalysts, where the activation of C–H bonds was found to be much easier than that of C–C bonds under similar thermodynamic conditions.

More importantly, the trend shown in Figure 4 can qualitatively explain the rapid deactivation of the traditional Ni catalyst due to carbon deposition in the methanreforming

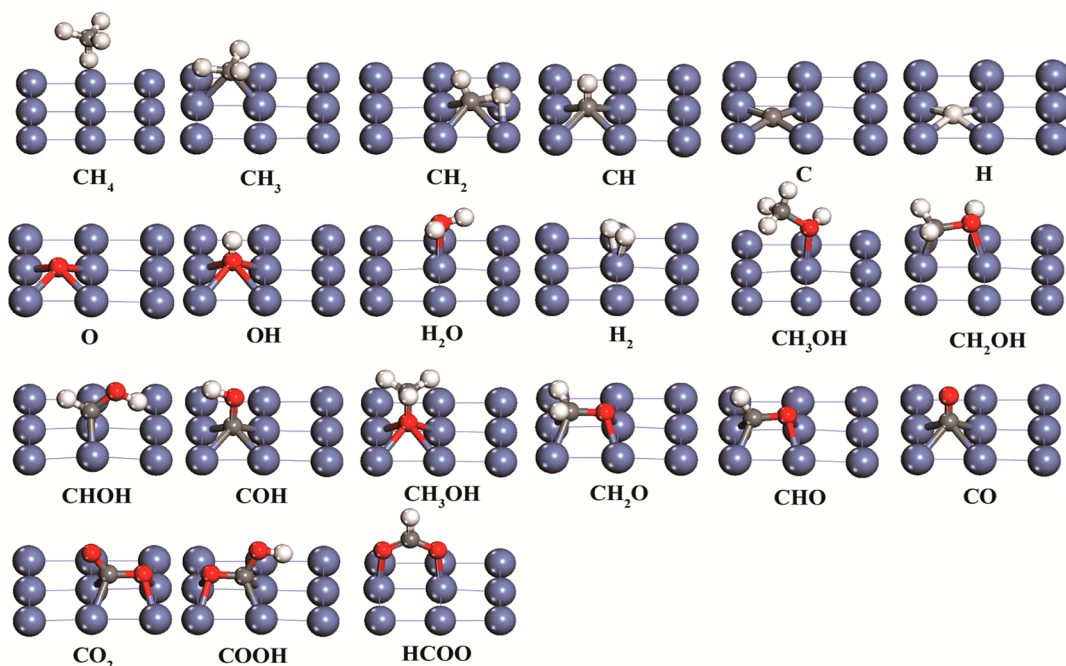


Figure 2. Adsorption configurations in DRM on Ni(100). The blue balls denote Ni atoms; the black balls denote C atoms; the red balls denote O atoms; the white balls denote H atoms.

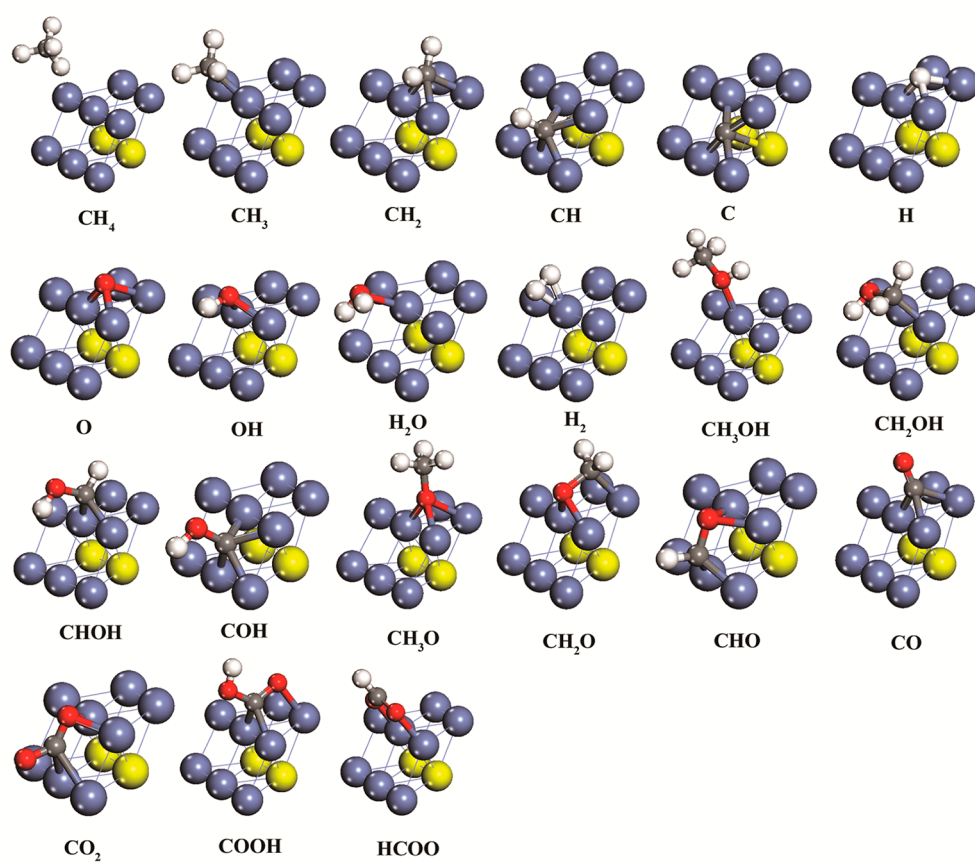


Figure 3. Adsorption configurations in DRM on Ni(211).

reactions. From the figure we know that the activation energies for the C–O bond-formation reactions are generally higher than those for the C–H bond-breaking reactions on Ni surfaces. Given the relatively high methane partial pressure

under realistic conditions, the oxidation reactions are likely to be slower than the dehydrogenation reactions. This would lead to the accumulation of the deeply dehydrogenated species such as CH and C on the catalyst surface, which are commonly

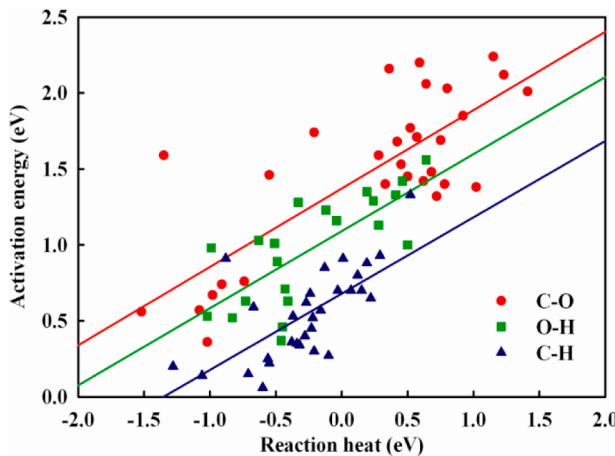


Figure 4. Plot of the activation energy against the reaction heat. The red, green, and blue symbols correspond to the C–O, O–H, and C–H bond-making (or bond-breaking) reactions, respectively.

suggested to be the precursors of carbon formation.⁴⁴ Therefore, in order to improve the stability of the catalysts in the methane reforming reactions, the increase in the rates for oxidation reactions and the decrease in the rates for dehydrogenation reactions are simultaneously desired. Experimentally, a practical method to inhibit carbon formation during steam methane reforming is to increase the steam-to-carbon ratio,^{45,46} so that the surface coverage of O and OH species are increased and the oxidation reactions are promoted accordingly. Another approach is to partially passivate the Ni catalyst by preadsorption of sulfur atoms on the corrugated surfaces,⁴⁷ or alloying Ni catalysts with some other elements,⁴⁸ which is supposed to reduce the dehydrogenation reaction rates.

3.2. Microkinetic Model. 3.2.1. Rate Constant. Once the activation energies for the forward and reverse elementary reactions in the DRM process are obtained, the reaction constants can be estimated based on statistical mechanics treatments and transition state theory:

$$k = \frac{k_b T}{h} \exp\left(\frac{\Delta S^\ddagger}{R}\right) \exp\left(-\frac{\Delta H^\ddagger}{RT}\right) \quad (2)$$

where k is the reaction constant; k_b is Boltzmann's constant; h is Planck's constant; ΔS^\ddagger is the entropy change from the reactant to the transition state complex; ΔH^\ddagger is the enthalpy change from the reactant to the transition state complex; R is the universal gas constant; T is the reaction temperature. The detailed formulas to derive the enthalpy and entropy at finite temperatures and pressures can be found in our previous publication.²⁸

For a general elementary reaction $A + B \rightleftharpoons C + D$, the overall reaction rate on the three Ni surfaces [Ni(111), Ni(100), and Ni(211)] can be written as,

$$r = \sum_{i=1}^3 [(k_{f,i} n_{A,i} n_{B,i} - k_{r,i} n_{C,i} n_{D,i}) N_{\text{site},i}] 3600 \quad (3)$$

where the r is the net reaction rate; $k_{f,i}$ and $k_{r,i}$ are the forward and reverse rate constant on surface i , respectively; n_i is the concentration of the reactants or products on surface i ; $N_{\text{site},i}$ is the number of the active sites on surface i .

Since three different facets of Ni catalyst are considered in this work, it is essential to estimate the contribution of each surface to the overall reaction kinetics. The Ni catalyst particle can be represented as a truncated octahedron which is surrounded by Ni(111) and Ni(100) with Ni(211) acting as the border region. Under this definition, the proportion of each type of surface atoms can be estimated. For a Ni particle of around 7 nm in size, the proportions are 0.74, 0.15, and 0.11 for Ni(111), Ni(100), and Ni(211), respectively.²¹ With the assumption of a fast surface diffusion process for all adsorbed species, the concentrations of the intermediates on all the surfaces are identical. This assumption is reasonable because the diffusion barriers are generally smaller than the energy barriers for surface reactions. Then, eq 3 can be rearranged as

$$r = \sum_{i=1}^3 \left[\left(k_{f,i} \frac{N_{\text{site},i}}{N_{\text{site},\text{total}}} n_A n_B - k_{r,i} \frac{N_{\text{site},i}}{N_{\text{site},\text{total}}} n_C n_D \right) \right] N_{\text{site},\text{total}} 3600 \quad (4)$$

where the $N_{\text{site},\text{total}}$ is the total number of active sites counting over all the three surfaces. On substituting the proportion of each surface into eq 3, the overall rate constants for the elementary reactions can be expressed as

$$k_f = \sum_{i=1}^3 k_{f,i} \frac{N_{\text{site},i}}{N_{\text{site},\text{total}}} = 0.74 k_{f,111} + 0.15 k_{f,100} + 0.11 k_{f,211} \quad (5)$$

$$k_r = \sum_{i=1}^3 k_{r,i} \frac{N_{\text{site},i}}{N_{\text{site},\text{total}}} = 0.74 k_{r,111} + 0.15 k_{r,100} + 0.11 k_{r,211} \quad (6)$$

where the k_f and k_r are the overall forward and reverse rate constants for the elementary reactions, respectively; $k_{f,111}$ and $k_{r,111}$ are the forward and reverse rate constants for the elementary reactions on Ni(111), respectively; the other symbols are defined in a similar way. The reaction constants are calculated and summarized in the Supporting Information (see Table S3) for the DRM reaction at a temperature of 973.15 K. It should be mentioned that CH_4 adsorption is a physisorption with a low adsorption energy of -0.02 eV, so that the adsorption and dissociation of CH_4 can be described in one single step. The combination of two chemisorbed H to H_2^* and the desorption H_2^* is also represented in one single step for the same reason. In addition, the possibilities of the adsorption and desorption reactions of methanol (CH_3OH) are disregarded in the microkinetic model because no CH_3OH has been detected under experimental conditions.

3.2.2. Kinetic Model. As illustrated above, there are five gas-phase molecules and 19 surface species (20 if vacant sites are included) involved in the DRM reaction. According to the steady-state approximation, we have,

$$\frac{d\theta_i}{dt} = \sum_{i=1}^{20} \sigma_i r_i = 0 \quad (7)$$

where θ_i is the surface coverage of species i , σ_i is the stoichiometric coefficient, r_i is the net reaction rate for species i , and t is time. According to the “flowing surface species approximation” (FSSA),⁴⁹ eq 7 can be rewritten as,

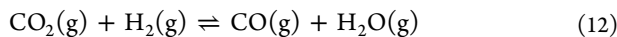
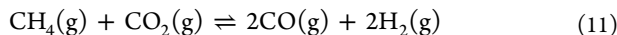
$$\frac{d\theta_i}{d(W/E_0)} = \sum_{i=1}^{20} \sigma_i r_i \quad (8)$$

where W is the weight of the catalyst and F_0 is the initial molar flow rate of the reactants. If the reaction takes place in an ideal PFR reactor which is a reasonable simplification for a typical fixed-bed reactor, the conversion of CH_4 and CO_2 as a function of space time can be written as,

$$\frac{dx_{\text{CH}_4}}{d(W/F_{\text{CH}_4,0})} = r_1 \quad (9)$$

$$\frac{dx_{\text{CO}_2}}{d(W/F_{\text{CO}_2,0})} = r_5 \quad (10)$$

where x_{CH_4} and x_{CO_2} are the conversion of CH_4 and CO_2 , r_1 and r_5 are the rates for reactions 1 and 5 in Supporting Information, Table S3. As for gas-phase CH_4 , CO_2 , CO , H_2 , and H_2O , the volume fraction initially present are defined as $y_{\text{CH}_4,\text{in}}$, $y_{\text{CO}_2,\text{in}}$, $y_{\text{CO},\text{in}}$, $y_{\text{H}_2,\text{in}}$, and $y_{\text{H}_2\text{O},\text{in}}$. There are two overall reactions involved in the DRM reaction,



Since the DRM process is a variable-volume gas-phase reaction, the partial pressure of the gas-phase molecules can be correlated with x_{CH_4} and x_{CO_2} based on C, O, and H balance, which can be expressed as,

$$P_{\text{CH}_4} = \frac{y_{\text{CH}_4,\text{in}}(1 - x_{\text{CH}_4})}{1 + 2y_{\text{CH}_4,\text{in}}x_{\text{CH}_4}} \times P_{\text{total}} \quad (13)$$

$$P_{\text{CO}_2} = \frac{y_{\text{CO}_2,\text{in}}(1 - x_{\text{CO}_2})}{1 + 2y_{\text{CH}_4,\text{in}}x_{\text{CH}_4}} P_{\text{total}} \quad (14)$$

$$P_{\text{CO}} = \frac{y_{\text{CO},\text{in}} + y_{\text{CH}_4,\text{in}}x_{\text{CH}_4} + y_{\text{CO}_2,\text{in}}x_{\text{CO}_2}}{1 + 2y_{\text{CH}_4,\text{in}}x_{\text{CH}_4}} P_{\text{total}} \quad (15)$$

$$P_{\text{H}_2} = \frac{y_{\text{H}_2,\text{in}} + 3y_{\text{CH}_4,\text{in}}x_{\text{CH}_4} - y_{\text{CO}_2,\text{in}}x_{\text{CO}_2}}{1 + 2y_{\text{CH}_4,\text{in}}x_{\text{CH}_4}} P_{\text{total}} \quad (16)$$

$$P_{\text{H}_2\text{O}} = \frac{y_{\text{H}_2\text{O},\text{in}} - y_{\text{CH}_4,\text{in}}x_{\text{CH}_4} + y_{\text{CO}_2,\text{in}}x_{\text{CO}_2}}{1 + 2y_{\text{CH}_4,\text{in}}x_{\text{CH}_4}} P_{\text{total}} \quad (17)$$

where P_{total} is the total pressure.

3.2.3. Thermodynamic Consistency. To obtain reasonable results from microkinetic modeling, the DFT-calculated thermodynamics for the DRM reaction should be consistent with the experimental values. As for the two overall reactions shown in eqs 11 and 12, the activation energies and pre-exponential factors should follow the relationship as,⁵⁰

$$\sum_i \sigma_i(E_{i,f}) - \sum_i \sigma_i(E_{i,r}) = \Delta H_{\text{net}}^0 \quad (18)$$

$$\prod_i \left(\frac{A_{i,f}}{A_{i,r}} \right)^{\sigma_i} = \exp \left(\frac{\Delta S_{\text{net}}^0}{R} \right) \quad (19)$$

where the terms on the left-hand side of the two equations are the activation energies and the pre-exponential factors for the forward and reversed elementary reactions, which are derived

from our DFT calculations. The terms on the right-hand, ΔH_{net}^0 and ΔS_{net}^0 are the standard enthalpy change and entropy change for the overall reactions, which can be found in the CRC handbook.⁵¹ It is found that the DFT calculated values are 3.48 eV and 2.95×10^{-3} eV/K in eq 11 and 0.78 eV and 3.32×10^{-3} eV/K in eq 12. However, the corresponding experimental data from the CRC handbook are 2.70 eV, 2.95×10^{-3} eV/K and 0.36 eV, 3.32×10^{-3} eV/K. It can be seen that the calculated entropy change are in excellent agreement with the experimental values, while the calculated enthalpy changes are ~ 0.8 eV larger than the experimental values for eq 11 and ~ 0.4 eV for eq 12, respectively. This discrepancy is mainly due to the overestimate of the DFT-calculated adsorption heats, which would lead to a DFT-predicted equilibrium constant that is 7 orders of magnitude away from the expected value at 973.15 K. The previous work by Hammer et al. showed that the GGA-PBE functional generally overestimated the chemisorption energies of small molecules, and the variation could be up to ~ 0.6 eV.⁵² Hence, the adsorption energies of gas-phase molecules need to be adjusted to make the model consistent with the gas-phase thermochemistry. By comparing the DFT-calculated adsorption energies and the experimental values, it is found that the DFT-calculated CO adsorption energy is around 0.4 eV more negative than the experimental value, while the other adsorption energies are in reasonable agreement with the experimental data.⁵³ Therefore, the adsorption energy of CO in the microkinetic model is reduced by 0.4 eV so that the thermodynamic consistency of the microkinetic model is maintained.

3.2.4. Microkinetic Modeling. In our simulation, the DRM reaction is carried out at 973.15 K, 10 bar with the BET area of Ni catalyst of $7.2 \text{ m}^2/\text{g}$ and the initial volume fractions of CH_4 and CO_2 being 0.5 and 0.5, respectively. The value of W/F_0 is set to be 0.01 g_{cat}·h/mol, which gives rise to low conversions of CH_4 and CO_2 and thus minor gradients in concentration and temperature down the catalyst bed. Under these experimental conditions, the differential eqs 8–10 can be solved with the ODE15s method as implemented in MATLAB. After solving the microkinetic model, the surface coverages of reaction intermediates and reaction rates for elementary reactions are obtained, as presented in Tables 2 and 3. From Table 2, it can be seen that CO has the highest surface coverage among all the reacting species and thus the most abundant reaction intermediates (MARI) on the surface. The coverages of other species are in the following order: H > C > O > CH > OH, and the contributions from the remaining surface species are negligible.

The conversion of CH_4 and CO_2 (x_{CH_4} and x_{CO_2}) can be also obtained from the modeling results, which are calculated to be 15.9% and 37.8%. The mole fractions of the reactants and products are 0.36, 0.27, 0.23, 0.04, and 0.10 for CH_4 , CO_2 , CO , H_2 , and H_2O , respectively, in the exit stream from the reactor. Here the conversion of CO_2 is higher than that of CH_4 and the yield of CO is higher than that of H_2 in the products, which suggests that the resultant H_2 via DRM reacts further with CO_2 through the RWGS reaction to produce CO and H_2O . The simulation results are in reasonable agreement with the experimental findings that the DRM reaction is accompanied by the RWGS reaction.¹¹

3.3. Microkinetic Analysis. **3.3.1. Reaction Pathways and Rate-Determining Steps.** The forward reaction rates for the elementary reactions under the reaction conditions are

Table 2. Surface Coverage of Adsorbates in DRM Reaction ($W/F_0 = 0.01 \text{ g}_{\text{cat}} \cdot \text{h/mol}$)

no.	species	coverage
1	CH_3	9.98×10^{-7}
2	CH_2	3.21×10^{-6}
3	CH	1.19×10^{-3}
4	C	1.69×10^{-2}
5	H	5.71×10^{-2}
6	O	2.40×10^{-3}
7	OH	6.13×10^{-5}
8	H_2O	2.66×10^{-6}
9	CH_3OH	3.20×10^{-15}
10	CH_2OH	3.82×10^{-14}
11	CHOH	4.11×10^{-12}
12	COH	2.09×10^{-7}
13	CH_3O	1.50×10^{-11}
14	CH_2O	1.36×10^{-11}
15	CHO	3.72×10^{-8}
16	CO	6.60×10^{-1}
17	CO_2	4.89×10^{-6}
18	COOH	6.47×10^{-10}
19	HCOO	3.78×10^{-8}
20	free site	2.63×10^{-1}

Table 3. Forward Reaction Rate for Elementary Reactions in DRM on Ni Catalyst ($\text{mol/g}_{\text{cat}} \cdot \text{h}$)

no.	elementary reaction	forward reaction rate
1	$\text{CH}_4(g) + 2^* = \text{CH}_3^* + \text{H}^*$	5.53×10^{02}
2	$\text{CH}_3^* + * = \text{CH}_2^* + \text{H}^*$	4.83×10^{03}
3	$\text{CH}_2^* + * = \text{CH}^* + \text{H}^*$	1.12×10^{06}
4	$\text{CH}^* + * = \text{C}^* + \text{H}^*$	3.89×10^{06}
5	$\text{CO}_2(g) + * = \text{CO}_2^*$	2.38×10^{07}
6	$\text{CO}_2^* + * = \text{CO}^* + \text{O}^*$	6.06×10^{02}
7	$\text{CO}_2^* + \text{H}^* = \text{COOH}^* + *$	1.25×10^{00}
8	$\text{CO}_2^* + \text{H}^* = \text{HCOO}^* + *$	6.22×10^{01}
9	$\text{HCOO}^* + * = \text{CHO}^* + \text{O}^*$	7.82×10^{-3}
10	$\text{COOH}^* + * = \text{CO}^* + \text{OH}^*$	4.00×10^{00}
11	$\text{CH}_3^* + \text{OH}^* = \text{CH}_3\text{OH}^* + *$	1.77×10^{-5}
12	$\text{CH}_3\text{OH}^* + * = \text{CH}_2\text{OH}^* + \text{H}^*$	4.18×10^{-6}
13	$\text{CH}_2^* + \text{OH}^* = \text{CH}_2\text{OH}^* + *$	8.35×10^{-4}
14	$\text{CH}_2\text{OH}^* + * = \text{CHOH}^* + \text{H}^*$	7.54×10^{-3}
15	$\text{CH}^* + \text{OH}^* = \text{CHOH}^* + *$	5.76×10^{-2}
16	$\text{CHOH}^* + * = \text{COH}^* + \text{H}^*$	1.61×10^{01}
17	$\text{C}^* + \text{OH}^* = \text{COH}^* + *$	1.34×10^{00}
18	$\text{COH}^* + * = \text{CO}^* + \text{H}^*$	1.75×10^{03}
19	$\text{CH}_3^* + \text{O}^* = \text{CH}_3\text{O}^* + *$	3.72×10^{-4}
20	$\text{CH}_3\text{O}^* + * = \text{CH}_2\text{O}^* + \text{H}^*$	3.45×10^{-2}
21	$\text{CH}_2^* + \text{O}^* = \text{CH}_2\text{O}^* + *$	1.13×10^{-2}
22	$\text{CH}_2\text{O}^* + * = \text{CHO}^* + \text{H}^*$	4.87×10^{00}
23	$\text{CH}^* + \text{O}^* = \text{CHO}^* + *$	2.93×10^{00}
24	$\text{CHO}^* + * = \text{CO}^* + \text{H}^*$	2.37×10^{04}
25	$\text{C}^* + \text{O}^* = \text{CO}^* + *$	1.16×10^{01}
26	$\text{CH}_3\text{OH}^* + * = \text{CH}_3\text{O}^* + \text{H}^*$	4.12×10^{-3}
27	$\text{CH}_2\text{OH}^* + * = \text{CH}_2\text{O}^* + \text{H}^*$	1.42×10^{-3}
28	$\text{CHOH}^* + * = \text{COH}^* + \text{H}^*$	1.61×10^{-01}
29	$\text{O}^* + \text{H}^* = \text{OH}^* + *$	3.74×10^{03}
30	$\text{OH}^* + \text{H}^* = \text{H}_2\text{O}^* + *$	3.12×10^{02}
31	$\text{H}_2\text{O}^* = \text{H}_2\text{O}(g) + *$	7.07×10^{06}
32	$\text{H}^* + \text{H}^* = \text{H}_2(g) + 2^*$	2.04×10^{05}
33	$\text{CO}^* = \text{CO}(g) + *$	4.80×10^{05}

calculated and listed in Table 3. Having calculated the forward reaction rate for all the elementary reactions involved in DRM, we are now in the position to analyze the dominant reaction pathway for the whole process. Here we identified the dominant reaction pathway in a complex reaction network according to the method proposed by Fishtik and Datta. The details of this method can be found in a series of their publications and the references therein.^{54,55}

The present microkinetic model involving $q = 19$ surface intermediates and $p = 33$ elementary reactions, as listed in Table 3. Hence, an overall reaction route involves at most $q + 1 = 20$ elementary reactions. Because the adsorption and desorption of the reactants and products in the DRM reaction (Table 3, reactions 1, 5, 32, and 33) are essential to any of reaction routes, the total number of the reaction routes would not exceed the number of ways $20 - 4 = 16$ elementary reactions might be selected from the $33 - 4 = 29$ reactions, that is, $29! / 16! / 13! \approx 6.79 \times 10^{07}$. Then these reaction routes are further screened to ensure that the correct overall reaction equation for DRM is yielded. For each reaction route, the elementary reaction with the slowest forward reaction rate is defined as the RDS. On the basis of this approach and the calculated forward reaction rate for all the elementary reactions, the dominant reaction pathway and corresponding RDS can be identified.

Adsorption and Desorption of Gaseous Species. From Table 3, one can see that the forward reaction rates for adsorption of the reactants and desorption of the products are of the order of magnitude of 10^3 – $10^6 \text{ mol/g}_{\text{cat}} \cdot \text{h}$, which indicates that these reactions are rather fast and can readily reach equilibrium.

CH_4 Activation: Dehydrogenation vs Oxidation. As for one of the reactants, CH_4 can be successively dissociated to form CH_x ($x = 1$ – 3) fragments and atomic H (including reactions 2–4 in Table 3), which are oxidized by surface O or OH species, and the resulting oxides such as CH_xO or CH_xOH are subsequently decomposed (including reactions 11–24 and 26–28, respectively). From Table 3, it can be seen that the forward rates for the dehydrogenation reactions are of the order of magnitude of 10^3 – $10^6 \text{ mol/g}_{\text{cat}} \cdot \text{h}$ while the forward rates for the oxidation reactions of CH_x by O and OH are of the order of magnitude of 10^{-4} – 10^0 and 10^{-5} – $10^{-2} \text{ mol/g}_{\text{cat}} \cdot \text{h}$, respectively. Apparently the dehydrogenation reactions are much faster than the corresponding oxidation reactions, which can be rationalized as follows. On one hand, as discussed above, the activation energies for the dehydrogenation reactions are generally lower than those for the oxidation reactions (see Supporting Information, Table S1 and Figure 4), and therefore the corresponding rate constants are higher (see Supporting Information, Table S3), given that the pre-exponential factors for surface reactions are rather close. On the other hand, the coverage of free surface sites is much higher than those of surface O and OH. It is these two factors that make dehydrogenation reactions kinetically more favorable than oxidation reactions.

CO_2 Activation: Direct Decomposition vs COOH or HCOO Pathway. As for the other reactant CO_2 , the activation of the C–O bond has three different pathways: (i) direct decomposition to form CO and O (reaction 6 in Table 3); (ii) combination with H to form COOH or HCOO (reactions 7 and 8 in Table 3), which can be further decomposed into CO and OH or CHO and O (reactions 9 and 10 in Table 3). By comparing the reaction rates for these reactions, one can see

that the forward rate for reaction 6 is 484 times faster than that for reaction 7 and 10 times faster than that for reaction 8, implying that the direct decomposition is the dominant reaction pathway, while the HCOO pathway contributes to a much less extent and the COOH pathway could be negligible.

Source of Oxidants. According to the previous results, one can see that the oxidants for the DRM process are surface O or OH species. The surface O arises apparently from the decomposition of CO₂. However, the surface OH can be either from the decomposition of COOH (Table 3, reaction 7) or from the hydrogenation of O by H (Table 3, reaction 29). From Table 3, it is apparent that the forward rate for reaction 29 is much higher than that for reaction 7, suggesting that the surface OH arises mainly from the hydrogenation of surface O atoms.

CO Formation. CO can be formed via several different reaction pathways. From the aforementioned analysis, it can be deduced that the oxidation of carbon-containing species cannot occur until all the C–H bonds are broken to form atomic C. Once atomic C is formed, it can be further oxidized by the surface O or OH species. Here three reaction pathways are taken into account. Along the first reaction pathway, atomic C is oxidized by surface O to form CO (reaction 25 in Table 3), which is denoted as PATH(I). Along the second reaction pathway denoted as PATH(II), C is oxidized by surface OH to form COH (reaction 17), which can be further decomposed into CO and H (reaction 18). It can be seen from Table 3 that the reaction rates for these two reactions are quite close (of the same order of magnitude), and therefore both of these two reaction pathways might contribute to the overall reaction. In addition, it should be noted that atomic C can also be hydrogenated to yield CH. Hence, one can find another reaction pathway with CH oxidized by O to form CHO (reaction 23) which can be further decomposed into CO and H (reaction 24) [denoted as PATH(III)]. The forward rate for this reaction is also quite close to those for the aforementioned two reaction pathways, and therefore this pathway also plays a role within the overall reaction network. The oxidation steps, namely, reactions 25, 17, and 23, are the slowest steps along the three reaction pathways and considered as the RDSs for PATH(I), PATH(II), and PATH(III), respectively.

Reaction Pathways. Finally, three reaction pathways with comparable forward reaction rates are identified for the DRM process, as illustrated in Figure 5. The forward reaction rates for

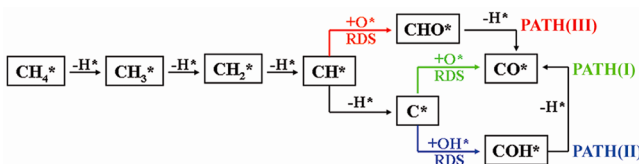


Figure 5. Dominant reaction pathways and rate-determining steps in DRM over Ni catalyst.

the RDSs along PATH(I), PATH(II), and PATH(III) are calculated to be 11.6, 1.34, and 2.93 mol/g_{cat}·h, respectively (see Table 3). The contribution of each reaction pathway (C_i) can be calculated simply by neglecting the reverse reactions of the RDSs,

$$C_i = \frac{r_{\text{RDS},i}}{\sum_{i=1}^3 r_{\text{RDS},i}} \quad (20)$$

where $r_{\text{RDS},i}$ is the forward reaction rate for the RDS along the reaction pathway i . The calculated C_i for the three reaction pathways are 73.1%, 8.4%, and 18.5%, respectively, which indicatess that PATH(I) is the dominant reaction pathway and PATH(II) and PATH(III) contribute to the overall reaction to a less extent. Along these three reaction pathways, the oxidation of C and CH are the slowest steps and are therefore suggested to be the RDSs for the DRM process, which dominate the overall reaction rate.

3.3.2. Surface Coverage Effect. It is worth noting that the surface coverages of the reaction intermediates may affect the calculated adsorption energies and activation energies through adsorbate–adsorbate interactions, which in turn might have an effect on the simulated results. Although our calculations are performed at a low surface coverage (0.11 ML) without any coadsorbates, we may briefly deduce the coverage dependence of the reaction kinetics on the basis of the understandings achieved in sections 3.1 and 3.2. As aforementioned, a stronger binding of reaction intermediates could promote bond-breaking reactions such as the dehydrogenation reactions, while a weaker binding strength would benefit bond-formation reactions. The increase in the surface coverage is suggested to reduce the binding ability of catalyst surface to reaction intermediates, which arises from the lateral interactions, and consequently, the oxidation reactions are promoted while the dehydrogenation reactions are kinetically hindered. Therefore, at high surface coverages, the RDS would probably change from the oxidation reactions to the dehydrogenation reactions.

3.3.3. Catalyst Deactivation. In experiments, carbon deposition on the Ni catalyst is severe under the reforming conditions, which would lead to a rapid deactivation of the catalyst.^{3,4} Because the adsorption energies of C atoms on Ni(100) and Ni(211) are more negative than that on Ni(111), indicating higher affinities of C at these under-coordinated sites, these surface sites might be blocked by C atoms and the active sites for the activation of CH_4 and CO_2 could move from the stepped sites to the flat terrace sites, so that the DRM reaction was modeled on Ni(111) without the contributions from Ni(100) and Ni(211) as well to shed light on the effect of catalyst deactivation on the reaction mechanism.

Here we compared the forward reaction rates of reaction 1 [$\text{CH}_4(\text{g}) + 2* = \text{CH}_3^* + \text{H}^*$] and reaction 25 ($\text{C}^* + \text{O}^* = \text{CO}^* + *$). As listed in Table 3, the forward reaction rates for these two reactions are calculated to be 553 and 12 mol/g_{cat}·h with the contributions from all the three facets on Ni catalyst. When the Ni(100) and Ni(211) surfaces are deactivated, the forward reaction rates for these two reactions are calculated to be 731 and 0.1 mol/g_{cat}·h, which suggests that the oxidation of atomic C remains the RDS for the DRM reaction. Carefully examining the simulated results may rationalize the variation in the reaction rates for the two reactions. On one hand, the reaction constant for reaction 1 decreases because of its much higher activation energy on Ni(111). On the other hand, the coverage of free surface sites significantly increases because of the weak binding ability of Ni(111) to the reaction intermediates. The dominant increase in the coverage of free surface sites finally gives rise to an increase in the reaction rate for reaction 1. For reaction 25, the rate constant is increased owing to the lower activation energy on Ni(111) than those on the other two facets. The coverages of the C^* and O^* species, however, are decreased due to their weaker binding strength on Ni(111). These two opposite trends give rise to an overall decreased reaction rate for reaction 25, which indicates that the

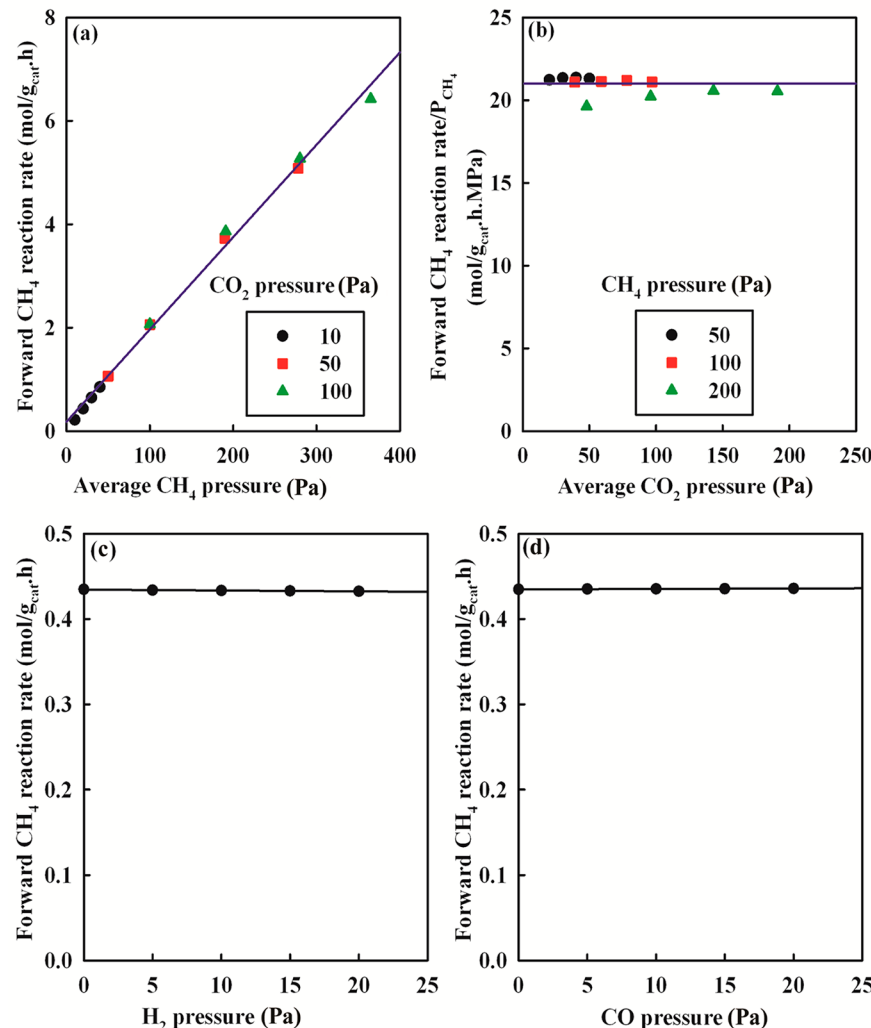


Figure 6. Effects of CH_4 (a), CO_2 (b), H_2 (c), and CO (d) partial pressures on the forward CH_4 reaction rate for DRM reaction at low pressures. In panels c and d, 0–20 Pa H_2 and CO are added to the reactant mixture of 20 Pa CH_4 and 20 Pa CO_2 .

Table 4. Comparison of the Forward Reaction Rate for Reaction 25 to That for CH_4 Dissociation at Various Temperatures and Total Pressures

pressure	reaction	forward reaction rate				
		823 K	873 K	923 K	973 K	1023 K
20 Pa	$\text{CH}_4(\text{g}) + 2^* = \text{CH}_3^* + \text{H}^*$ (reaction 1)	9.08×10^{00}	1.68×10^{01}	2.64×10^{01}	3.57×10^{01}	4.25×10^{01}
	$\text{C}^* + \text{O}^* = \text{CO}^* + *$ (reaction 25)	3.19×10^{00}	7.58×10^{00}	1.34×10^{01}	1.97×10^{01}	2.37×10^{01}
	$r_{1,f}/r_{25,f}$	2.85	2.22	1.97	1.81	1.79
10 bar	$\text{CH}_4(\text{g}) + 2^* = \text{CH}_3^* + \text{H}^*$ (reaction 1)	1.03×10^{01}	4.07×10^{01}	1.60×10^{02}	5.53×10^{02}	1.60×10^{03}
	$\text{C}^* + \text{O}^* = \text{CO}^* + *$ (reaction 25)	4.98×10^{-01}	1.95×10^{00}	4.34×10^{00}	1.16×10^{01}	3.44×10^{01}
	$r_{1,f}/r_{25,f}$	20.68	20.87	36.87	47.67	46.51

surface coverages may play a more significant role in determining the reaction rates.

3.3.4. Comparison to Available Experimental Data.
3.3.4.1. Effect of Partial Pressure. Wei and Iglesia demonstrated through experiment that the forward CH_4 reaction rate increases linearly with increasing CH_4 partial pressure but it is not influenced by the CO_2 , H_2 , and CO partial pressures in the DRM reaction, and therefore they suggested that the dissociation of CH_4 is the RDS for the DRM reaction.¹⁰ To compare our simulated results to experimental data, we performed the microkinetic modeling for the DRM reaction

at very low total pressures ranging from 20 to 800 Pa at 973.15 K. The calculated forward reaction rate for CH_4 dissociation as a function of the CH_4 , CO_2 , H_2 , and CO partial pressures is illustrated in Figure 6 panels a, b, c, and d, respectively. Here the average CH_4 and CO_2 pressures are averaged over the data measured at the inlet and outlet of the reactor. It is apparent that the forward CH_4 reaction rate increases linearly with increasing CH_4 partial pressure, but it is not influenced by the CO_2 , H_2 , and CO partial pressures, which indicates that the present microkinetic model predicts exactly the same trends as

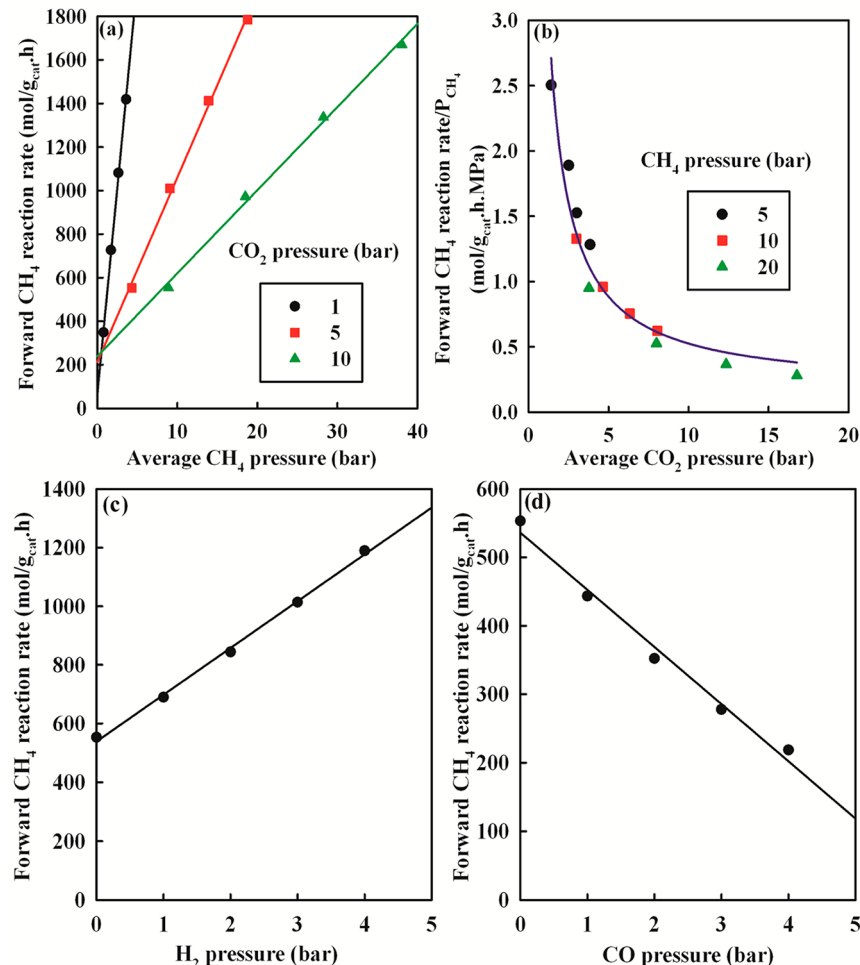


Figure 7. Effects of CH_4 (a), CO_2 (b), H_2 (c), and CO (d) partial pressures on the forward CH_4 reaction rate for DRM at high pressures. In panels c and d, 1–4 bar H_2 and CO are added to the reactant mixture of 5 bar CH_4 and 5 bar CO_2 .

those of Wei and Iglesia and CH_4 dissociation is the RDS for DRM at low pressures.

To identify the RDS for DRM at low pressures directly through the comparison of the forward reaction rates, the calculated data for reaction 25 that is evidenced to be kinetically relevant for the dominant PATH(I) at high pressures (see section 3.3.1) are given in Table 4. It can be seen from the table that the forward rates for reaction 25 are rather close to those for CH_4 dissociation at low pressures. For example, the ratio $r_{1,f}/r_{25,f}$ is only 1.81 at 20 Pa and 973.5 K. Considering the inherent limitations in DFT calculations, it is reasonable to conclude that both the dissociation of CH_4 and the oxidation of C^* are the RDSs for the DRM reaction at low pressures.

As mentioned in the Introduction, some other groups suggested different RDSs for the DRM reaction. For instance, Luo et al. suggested that the decomposition of CH_xO is the RDS on the basis of the pulse experiments and chemical trapping on a $\text{Ni}/\text{La}_2\text{O}_3$ catalyst.¹⁵ As another example, Chang et al. proposed that the oxidation step of surface carbon by oxygen is the RDS in the DRM reaction through isotope experiments on a supported KNiCa catalyst.¹² It should be noted that the experiments by Luo et al. and Chang et al. were carried out under atmospheric pressure. Therefore, it is reasonable to expect that the operating pressure might have an effect on the reaction mechanism. Here the microkinetic modeling was performed at 973.15 K and pressures ranging

from 1 to 20 bar to elucidate the effects of the CH_4 , CO_2 , H_2 , and CO partial pressures on the forward CH_4 reaction rate, as shown in Figures 7.

It is apparent that the effects of the partial pressures at high pressures are significantly different from those at low pressures. While the forward CH_4 reaction rate still increases linearly with increasing CH_4 partial pressure, the CO_2 pressure has a negative effect on the forward CH_4 reaction rate. The simulated results showed that at the CO_2 average pressure of 1.41 bar, the coverages of CO^* and free sites are calculated to be 0.53 and 0.36, respectively. When the average pressure of CO_2 is increased to 16.77 bar, the coverages of CO^* and free sites are calculated to be 0.83 and 0.12, respectively, which indicates that the high coverage of CO^* arising from the decomposition of CO_2 would block the surface free sites and thus lower the forward CH_4 reaction rate.

Although the H_2 pressure has negligible effect on the forward CH_4 reaction rate at low pressures, it has a positive effect on the forward CH_4 reaction rate at high pressures, as shown in Figure 7c. The coverages of CO^* and free sites are calculated to be 0.64 and 0.27 at the H_2 pressure of 1 bar, while the corresponding values are 0.59 and 0.31 at the H_2 pressure of 4 bar. This is because the increase in the H_2 pressure would promote the hydrogenation reactions, so that the CO^* coverage is lowered and the free site coverage is increased accordingly. On the other hand, the high H_2 pressure would

substantially lower the conversion of CH₄. The CH₄ partial pressure increases from 4.17 bar at the H₂ pressure of 1 to 5.73 bar at the H₂ pressure of 4 bar. Hence, the increased CH₄ forward reaction rate at high H₂ pressures can be rationalized according to these two effects.

The forward CH₄ reaction rate decreases with increasing CO pressure. For example, the CH₄ partial pressure increases from 3.88 bar at the CO pressure of 1 to 4.43 bar at the CO pressure of 4 bar. This is because the strongly chemisorbed CO* on Ni surfaces could easily occupy the surface free sites. The coverages of CO* and free sites are calculated to be 0.70 and 0.23 at the CO pressure of 1 bar, while the corresponding values are 0.80 and 0.15 at the CO pressure of 4 bar.

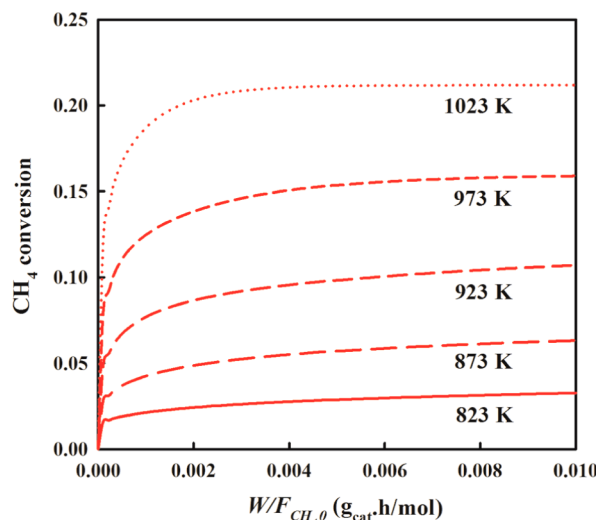


Figure 8. CH₄ conversion as a function of $W/F_{CH_4,0}$ at various reaction temperatures and at the total pressure of 10 bar.

3.3.4.2. Effect of Temperature. Figure 8 shows the conversion of CH₄ as a function of $W/F_{CH_4,0}$ at the temperature range of 823–1023 K and at the total pressure of 10 bar. The conversion of CH₄ increases from ~2% at 823 K to ~20% at 1023 K, which is in quantitative agreement with the previous experimental results by Xu and Froment.⁵⁶ The forward reaction rates for reactions 1 and 25 at different temperatures are also calculated and listed in Table 4. It is apparent from the table that at 20 Pa the ratios between the forward rates for the two reactions range from 1.79 to 2.85 as the reaction temperature is increased from 823 to 1023 K, and at 10 bar the corresponding values range from 20.68 to 40.67, indicating that the reaction temperature has a negligible effect on the reaction mechanism. At low pressures the difference in the forward reaction rate between reactions 1 and 25 holds almost constant at various temperatures, while at high pressures reaction 1 is even more promoted than reaction 25 at elevated reaction temperatures.

4. CONCLUSION

A comprehensive microkinetic model based on density functional calculations is constructed to explore the reaction mechanism for the DRM reaction over Ni catalyst. Three low-index facets, namely, Ni(111), Ni(100), and Ni(211) are utilized to represent the flat, open, and stepped surfaces,

respectively. The adsorption energies of all the possible reaction intermediates and the activation energies for the elementary reactions that are involved in the DRM reaction on the three Ni surfaces are obtained. It is found that the adsorption of the reaction intermediates are generally weaker on Ni(111) than that on the under-coordinated facets, and the adsorption energies on Ni(100) and Ni(211) are sensitive to the adsorption configurations. In general, the adsorptions at the atop and bridge sites are more favored on Ni(211), while the adsorptions at the hollow sites are preferred on Ni(100). For the bond-breaking reactions, the stronger the adsorption on the surface is, the lower is the activation energy, and vice versa for the bond-making reactions. For the C–O, O–H, and C–H bond-making (or bond-breaking) reactions, the BEP relation holds roughly true, and the kinetics of these reactions not only depends on the thermodynamics, but also is controlled by the intrinsic bond polarity.

The DFT-calculated results are further used to estimate the rate constants for the elementary reactions under realistic reaction temperatures and pressures within the framework of transition state theory and statistical mechanics treatments. With detailed microkinetic analysis, three dominant reaction pathways are identified for the DRM reaction over Ni catalyst, and the oxidation of the surface C or CH by the surface O or OH is found to be the RDSs. The contribution of each pathway is calculated to be 73.1%, 8.4%, and 18.5%, which indicates that the oxidation of C by O is the dominant reaction pathway.

With the comparison to the available experimental data, the effects of the partial pressure and reaction temperature on the reaction mechanism are discussed. At low CH₄ and CO₂ pressures, both CH₄ dissociative adsorption and CH or C oxidation would jointly dominate the overall reaction rate, while at high pressures CH or C oxidation is suggested as the RDS for the DRM reaction.

■ ASSOCIATED CONTENT

S Supporting Information

The activation energies, transition state structures, and rate constants for the elementary reactions involved in the DRM process. The Supporting Information is available free of charge on the ACS Publications website at DOI: 10.1021/acs.iecr.5b00563.

■ AUTHOR INFORMATION

Corresponding Authors

*E-mail: yan Zhu@ecust.edu.cn.

E-mail: chen@chemeng.ntnu.no.

Notes

The authors declare no competing financial interest.

■ ACKNOWLEDGMENTS

This work is supported by Natural Science Foundation of China (21303102, 21473053, 21403066), Fundamental Research Funds for Central Universities (WA1414043), and the China Postdoctoral Science Foundation (2014M561424). The computational time provided by the Notur project is highly acknowledged.

■ REFERENCES

- (1) Bachiller-Baeza, B.; Mateos-Pedrero, C.; Soria, M. A.; Guerrero-Ruiz, A.; Rodemerck, U.; Rodriguez-Ramos, I. Transient studies of low-temperature dry reforming of methane over Ni-CaO/ZrO₂-La₂O₃. *Appl. Catal., B* 2013, 129, 450–459.

- (2) Kahle, L. C. S.; Roussiére, T.; Maier, L.; Herrera Delgado, K.; Wasserschaff, G.; Schunk, S. A.; Deutschmann, O. Methane Dry Reforming at High Temperature and Elevated Pressure: Impact of Gas-Phase Reactions. *Ind. Eng. Chem. Res.* **2013**, *52*, 11920–11930.
- (3) Zhang, S. H.; Muratsugu, S.; Ishiguro, N.; Tada, M. Ceria-Doped Ni/SBA-16 Catalysts for Dry Reforming of Methane. *ACS Catal.* **2013**, *3*, 1855–1864.
- (4) Mette, K.; Kuhl, S.; Dudder, H.; Kahler, K.; Tarasov, A.; Muhler, M.; Behrens, M. Stable Performance of Ni Catalysts in the Dry Reforming of Methane at High Temperatures for the Efficient Conversion of CO₂ into Syngas. *ChemCatChem.* **2014**, *6*, 100–104.
- (5) Serrano-Lotina, A.; Daza, L. Influence of the Operating Parameters over Dry Reforming of Methane to Syngas. *Int. J. Hydrogen Energy* **2014**, *39*, 4089–4094.
- (6) Munera, J.; Irusta, S.; Cornaglia, L.; Lombardo, E.; Vargascesar, D.; Schmal, M. Kinetics and Reaction Pathway of the CO₂ Reforming of Methane on Rh Supported on Lanthanum-Based Solid. *J. Catal.* **2007**, *245*, 25–34.
- (7) Stagg-Williams, S. M.; Noronha, F. B.; Fendley, G.; Resasco, D. E. CO₂ Reforming of CH₄ over Pt/ZrO₂ Catalysts Promoted with La and Ce Oxides. *J. Catal.* **2000**, *194*, 240–249.
- (8) Verykios, X. Catalytic Dry Reforming of Natural Gas for the Production of Chemicals and Hydrogen. *Int. J. Hydrogen Energy* **2003**, *28*, 1045–1063.
- (9) Wang, S.; Li, Y.; Lu, J.; He, M.; Jiao, H. A Detailed Mechanism of Thermal CO₂ Reforming of CH₄. *J. Mol. Struct.* **2004**, *673*, 181–189.
- (10) Wei, J.; Iglesia, E. Isotopic and Kinetic Assessment of the Mechanism of Reactions of CH₄ with CO₂ or H₂O to Form Synthesis Gas and Carbon on Nickel Catalysts. *J. Catal.* **2004**, *224*, 370–383.
- (11) Bradford, M. C. J.; Vannice, M. A. CO₂ Reforming of CH₄. *Catal. Rev. - Sci. Eng.* **1999**, *41*, 1–42.
- (12) Chang, J.; Park, S.; Yoo, J.; Park, J. Catalytic Behavior of Supported KNiCa Catalyst and Mechanistic Consideration for Carbon Dioxide Reforming of Methane. *J. Catal.* **2000**, *195*, 1–11.
- (13) Cui, Y.; Zhang, H.; Xu, H.; Li, W. Kinetic Study of the Catalytic Reforming of CH₄ with CO₂ to Syngas over Ni/α-Al₂O₃ Catalyst: The Effect of Temperature on the Reforming Mechanism. *Appl. Catal., A* **2007**, *318*, 79–88.
- (14) Haghghi, M.; Sun, Z.; Wu, J.; Bromly, J.; Wee, H.; Ng, E.; Wang, Y.; Zhang, D. On the Reaction Mechanism of CO₂ Reforming of Methane over a Bed of Coal Char. *Proc. Combust. Inst.* **2007**, *31*, 1983–1990.
- (15) Luo, J. Z.; Yu, Z. L.; Ng, C. F.; Au, C. T. CO₂/CH₄ Reforming over Ni-La₂O₃/5A: An Investigation on Carbon Deposition and Reaction Steps. *J. Catal.* **2000**, *194*, 198–210.
- (16) Nandini, A.; Pant, K. K.; Dhingra, S. C. Kinetic Study of the Catalytic Carbon Dioxide Reforming of Methane to Synthesis Gas over Ni-K/CeO₂-Al₂O₃ Catalyst. *Appl. Catal., A* **2006**, *308*, 119–127.
- (17) Osaki, T.; Horiuchi, T.; Suzuki, K.; Mori, T. Kinetics, Intermediates and Mechanism for the CO₂-Reforming of Methane on Supported Nickel Catalysts. *J. Chem. Soc., Faraday Trans.* **1996**, *92*, 1627.
- (18) Osaki, T.; Mori, T. Role of Potassium in Carbon-Free CO₂ Reforming of Methane on K-Promoted Ni/Al₂O₃ Catalysts. *J. Catal.* **2001**, *204*, 89–97.
- (19) Bradford, M. C. J.; Vannice, M. A. Catalytic Reforming of Methane with Carbon Dioxide over Nickel Catalysts II. Reaction Kinetics. *Appl. Catal., A* **1996**, *142*, 97–122.
- (20) Blaylock, D. W.; Ogura, T.; Green, W. H.; Beran, G. J. O. Computational Investigation of Thermochemistry and Kinetics of Steam Methane Reforming on Ni(111) under Realistic Conditions. *J. Phys. Chem. C* **2009**, *113*, 4898–4908.
- (21) Blaylock, D. W.; Zhu, Y.-A.; Green, W. H. Computational Investigation of the Thermochemistry and Kinetics of Steam Methane Reforming Over a Multi-faceted Nickel Catalyst. *Top. Catal.* **2011**, *54*, 828–844.
- (22) Chen, D.; Lødeng, R.; Svendsen, H.; Holmen, A. Hierarchical Multiscale Modeling of Methane Steam Reforming Reactions. *Ind. Eng. Chem. Res.* **2011**, *50*, 2600–2612.
- (23) Wang, H. F.; Liu, Z. P. Comprehensive Mechanism and Structure-Sensitivity of Ethanol Oxidation on Platinum: New Transition-State Searching Method for Resolving the Complex Reaction Network. *J. Am. Chem. Soc.* **2008**, *130*, 10996–11004.
- (24) Studt, F.; Abild-Pedersen, F.; Bligaard, T.; Sorensen, R. Z.; Christensen, C. H.; Norskov, J. K. Identification of Non-Precious Metal Alloy Catalysts for Selective Hydrogenation of Acetylene. *Science* **2008**, *320*, 1320–1322.
- (25) Cao, X. M.; Burch, R.; Hardacre, C.; Hu, P. Reaction Mechanisms of Crotonaldehyde Hydrogenation on Pt(111): Density Functional Theory and Microkinetic Modeling. *J. Phys. Chem. C* **2011**, *115*, 19819–19827.
- (26) Cao, X. M.; Burch, R.; Hardacre, C.; Hu, P. An Understanding of Chemoselective Hydrogenation on Crotonaldehyde over Pt(111) in the Free Energy Landscape: The Microkinetics Study Based on First-Principles Calculations. *Catal. Today* **2011**, *165*, 71–79.
- (27) Wang, H. F.; Guo, Y. L.; Lu, G. Z.; Hu, P. NO Oxidation on Platinum Group Metals Oxides: First Principles Calculations Combined with Microkinetic Analysis. *J. Phys. Chem. C* **2009**, *113*, 18746–18752.
- (28) Zhu, Y. A.; Chen, D.; Zhou, X. G.; Yuan, W. K. DFT Studies of Dry Reforming of Methane on Ni Catalyst. *Catal. Today* **2009**, *148*, 260–267.
- (29) Kresse, G.; Furthmüller, J. Efficiency of Ab-Initio Total Energy Calculations for Metals and Semiconductors Using a Plane-Wave Basis Set. *Comput. Mater. Sci.* **1996**, *6*, 15–50.
- (30) Kresse, G.; Hafner, J. Ab Initio Molecular Dynamics for Liquid Metals. *Phys. Rev. B* **1993**, *47*, 558–561.
- (31) Kresse, G.; Hafner, J. Ab Initio Molecular-Dynamics Simulation of the Liquid-Metal-Amorphous-Semiconductor Transition in Germanium. *Phys. Rev. B* **1994**, *49*, 14251–14269.
- (32) Kresse, G.; Furthmüller, J. Efficient Iterative Schemes for Ab Initio Total-Energy Calculations Using a Plane-Wave Basis Set. *Phys. Rev. B* **1996**, *54*, 11169–11186.
- (33) Blöchl, P. E. Projector Augmented-Wave Method. *Phys. Rev. B* **1994**, *50*, 17953–17978.
- (34) Kresse, G.; Joubert, D. From Ultrasoft Pseudopotentials to the Projector Augmented-Wave Method. *Phys. Rev. B* **1999**, *59*, 1758–1775.
- (35) Perdew, J. P.; Burke, K.; Ernzerhof, M. Generalized Gradient Approximation Made Simple. *Phys. Rev. Lett.* **1996**, *77*, 3865–3868.
- (36) Monkhorst, H. J.; Pack, J. D. Special Points for Brillouin-Zone Integrations. *Phys. Rev. B* **1976**, *13*, 5188–5192.
- (37) Methfessel, M.; Paxton, A. T. High-Precision Sampling for Brillouin-Zone Integration in Metals. *Phys. Rev. B* **1989**, *40*, 3616–3621.
- (38) Zhu, Y. A.; Dai, Y. C.; Chen, D.; Yuan, W. K. First-Principles Study of Carbon Diffusion in Bulk Nickel during the Growth of Fishbone-Type Carbon Nanofibers. *Carbon* **2007**, *45*, 21–27.
- (39) Henkelman, G.; Jonsson, H. A Dimer Method for Finding Saddle Points on High Dimensional Potential Surfaces Using Only First Derivatives. *J. Chem. Phys.* **1999**, *111*, 7010–7022.
- (40) Sheppard, D.; Terrell, R.; Henkelman, G. Optimization Methods for Finding Minimum Energy Paths. *J. Chem. Phys.* **2008**, *128*, 134106.
- (41) Bronsted, J. N. Acid and Basic Catalysis. *Chem. Rev.* **1928**, *5*, 231–338.
- (42) Evans, M. G.; Polanyi, M. Inertia and Driving Force of Chemical Reactions. *Trans. Faraday Soc.* **1938**, *34*, 11–24.
- (43) Yang, M. L.; Zhu, Y. A.; Fan, C.; Sui, Z. J.; Chen, D.; Zhou, X. G. DFT Study of Propane Dehydrogenation on Pt Catalyst: Effects of Step Sites. *Phys. Chem. Chem. Phys.* **2011**, *13*, 3257–3267.
- (44) Snoeck, J. W.; Froment, G. F.; Fowles, M. Filamentous Carbon Formation and Gasification: Thermodynamics, Driving Force, Nucleation, and Steady-State Growth. *J. Catal.* **1997**, *169*, 240–249.
- (45) Lægsgaard Jørgensen, S.; Nielsen, P. E. H.; Lehrmann, P. Steam Reforming of Methane in a Membrane Reactor. *Catal. Today* **1995**, *25*, 303–307.

- (46) Wang, Y.; Chin, Y. H.; Rozmiarek, R. T.; Johnson, B. R.; Gao, Y.; Watson, J.; Tonkovich, A. Y. L.; Vander Wiel, D. P. Highly Active and Stable Rh/MgOAl₂O₃ Catalysts for Methane Steam Reforming. *Catal. Today* **2004**, *98*, 575–581.
- (47) Rostrup-Nielsen, J. R. Sulfur-Passivated Nickel Catalysts for Carbon-Free Steam Reforming of Methane. *J. Catal.* **1984**, *85*, 31–43.
- (48) Besenbacher, F.; Chorkendorff, I.; Clausen, B. S.; Hammer, B.; Molenbroek, A. M.; Nørskov, J. K.; Stensgaard, I. Design of a Surface Alloy Catalyst for Steam Reforming. *Science* **1998**, *279*, 1913–1915.
- (49) Joshi, P. V.; Kumar, A.; Mizan, T. I.; Klein, M. T. Detailed Kinetic Models in the Context of Reactor Analysis: Linking Mechanistic and Process Chemistry. *Energy Fuels* **1999**, *13*, 1135–1144.
- (50) Mhadeshwar, A. B.; Wang, H.; Vlachos, D. G. Thermodynamic Consistency in Microkinetic Development of Surface Reaction Mechanisms. *J. Phys. Chem. B* **2003**, *107*, 12721–12733.
- (51) Lide, D. R. CRC Handbook of Chemistry and Physics, 79th ed.; CRC Press: Boca Raton, FL, 1998.
- (52) Hammer, B.; Hansen, L. B.; Nørskov, J. K. Improved adsorption energetics within density-functional theory using revised Perdew-Burke-Ernzerhof functionals. *Phys. Rev. B* **1999**, *59*, 7413–7421.
- (53) Chen, D.; Lodeng, R.; Omdahl, K.; Anundskgs, A.; Olsvik, O.; Holmen, A. A Model for Reforming on Ni Catalyst with Carbon Formation and Deactivation. *Stud. Surf. Sci. Catal.* **2001**, *139*, 93–100.
- (54) Fishtik, I.; Datta, R. De Donder Relations in Mechanistic and Kinetic Analysis of Heterogeneous Catalytic Reactions. *Ind. Eng. Chem. Res.* **2001**, *40*, 2416–2427.
- (55) Fishtik, I.; Datta, R. UBI-QEP, a Microkinetic Model for the Water-Gas Shift Reaction on Cu(111). *Surf. Sci.* **2002**, *512*, 229–254.
- (56) Xu, J.; Froment, G. F. Methane Steam Reforming, Methanation and Water-Gas Shift: I. Intrinsic Kinetics. *AIChE J.* **1989**, *35*, 88–96.